

From pixels to camera

scaling superconducting nanowire single-photon detectors for imaging at the quantum-limit

Gao, Jun; Chang, Jin; Lopez-Rodriguez, Bruno; Zadeh, Iman Esmaeil; Zwiller, Val; Elshaari, Ali W.

DO

10.1186/s40580-025-00515-z

Publication date 2025

Document Version
Final published version

Published in Nano Convergence

Citation (APA)

Gao, J., Chang, J., Lopez-Rodriguez, B., Zadeh, I. E., Zwiller, V., & Elshaari, A. W. (2025). From pixels to camera: scaling superconducting nanowire single-photon detectors for imaging at the quantum-limit. *Nano Convergence*, *12*(1), Article 49. https://doi.org/10.1186/s40580-025-00515-z

Important note

To cite this publication, please use the final published version (if applicable). Please check the document version above.

Copyright

Other than for strictly personal use, it is not permitted to download, forward or distribute the text or part of it, without the consent of the author(s) and/or copyright holder(s), unless the work is under an open content license such as Creative Commons.

Takedown policy

Please contact us and provide details if you believe this document breaches copyrights. We will remove access to the work immediately and investigate your claim.

Green Open Access added to <u>TU Delft Institutional Repository</u> as part of the Taverne amendment.

More information about this copyright law amendment can be found at https://www.openaccess.nl.

Otherwise as indicated in the copyright section: the publisher is the copyright holder of this work and the author uses the Dutch legislation to make this work public.

ELSEVIER

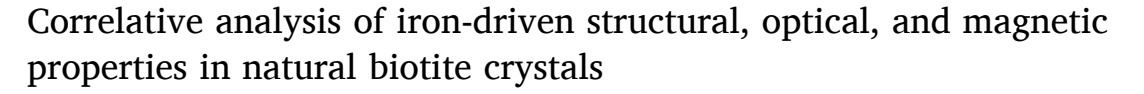
Contents lists available at ScienceDirect

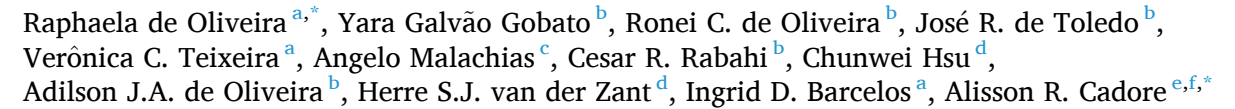
Applied Clay Science

journal homepage: www.elsevier.com/locate/clay



Research Paper





- a Brazilian Synchrotron Light Laboratory (LNLS), Brazilian Center for Research in Energy and Materials (CNPEM), 13083-970 Campinas, Sao Paulo, Brazil
- ^b Department of Physics, Federal University of São Carlos, 13565-905 São Carlos, São Paulo, Brazil
- ^c Department of Physics, Federal University of Minas Gerais, 31270-901 Belo Horizonte, Minas Gerais, Brazil
- d Kavli Institute of Nanoscience, Delft University of Technology, Lorentzweg 1, 2628 CJ Delft, the Netherlands
- e Brazilian Nanotechnology National Laboratory (LNNano), Brazilian Center for Research in Energy and Materials (CNPEM), 13083-970 Campinas, São Paulo, Brazil
- f Programa de Pós-Graduação em Física, Instituto de Física, Universidade Federal do Mato Grosso, 79070-900 Cuiabá, Mato Grosso, Brazil

ARTICLEINFO

Keywords: Phyllosilicates Biotites Iron oxidation states 2D heterostructures Magnetic substrate

ABSTRACT

Biotite crystals are phyllosilicate trioctahedral micas with the general chemical formula $K(Mg,Fe)_3AlSi_3O_{10}(OH)_2$ that form a solid-solution series with iron-poor phlogopite and iron-rich annite endmembers. With a wide band gap energy and a layered structure with free surface charges, biotite nanosheets can be readily obtained by cleavage methods and used as dielectrics in nanodevice fabrication for the next generation of electronics and energy harvesting. Here, a comprehensive study of biotite samples with different iron concentrations and oxidation states is presented. Structural, optical, magneto-optical, and magnetic characterizations were performed using several experimental techniques, including state-of-the-art synchrotron-based techniques, to correlate the iron chemistry (content and oxidation state) with the macroscopic properties of both minerals. The study reveals a nanoscale-homogeneous Fe distribution via synchrotron X-ray fluorescence mapping, defectmediated optical transitions modulated by Fe³⁺/Fe²⁺ ratios, and temperature-dependent magnetic transitions from paramagnetism to competing ferro-/antiferromagnetic interactions. Furthermore, the use of these biotite crystals as substrates for ultrathin heterostructures incorporating monolayer (ML) MoSe2 is explored by magneto photoluminescence at cryogenic temperatures. The results show that the presence of iron impurities in different oxidation states significantly impacts the valley properties for ML-MoSe2. Overall, these findings offer a comprehensive interpretation of the physical properties of bulk biotites in a correlative approach, serving as a robust reference for future studies aiming to explore biotites in their ultrathin form.

1. Introduction

One possible route for the future scaling of electronics is the integration of two-dimensional materials (2DMs) with existing silicon technology through the fabrication of thin nanosheet devices (Lemme et al., 2022; Zhu et al., 2023). Motivated by the development of this future hybrid electronic approach, researchers have investigated the fundamental properties and applications of several types of layered materials (LMs), including metallic and semimetallic ones (Novoselov et al., 2005; Craco et al., 2025), superconductors and semiconductors (Novoselov et al., 2005; Duan et al., 2015; Choi et al., 2017), as well as

insulating (Illarionov et al., 2020; Knobloch et al., 2021) and topological insulating (Kou et al., 2017; Culcer et al., 2020) LMs, most of which are synthesized by different routes. Although there are naturally occurring LMs (Frisenda et al., 2020), relatively little research has been carried out on natural insulating LMs compared to synthetic ones (Barcelos et al., 2023). The usual presence of defects and impurities (i.e., extra elements incorporated in the crystal lattice during the material formation) in naturally occurring LMs poses challenges for optimizing their properties for nanotechnology applications. On the other hand, they are abundant on Earth and easy to extract. Therefore, understanding defect engineering that enables their use in future nanotechnological applications

^{*} Corresponding authors at: Brazilian Center for Research in Energy and Materials (CNPEM), 13083-970 Campinas, São Paulo, Brazil. *E-mail addresses*: raphaela.goncalves@lnls.br (R. de Oliveira), alisson.cadore@lnnano.cnpem.br (A.R. Cadore).

could be the key to reducing overall costs (Fiori et al., 2014; Illarionov et al., 2020; de Oliveira et al., 2024b; Lopez-Richard et al., 2025).

Recently, there has been increasing interest in the physical properties of phyllosilicate minerals in their few-layer form (Barcelos et al., 2018; Mogg et al., 2019; Santos et al., 2019; Frisenda et al., 2020; Matković et al., 2021; Zou et al., 2021; Cadore et al., 2022; de Oliveira et al., 2023; Longuinhos et al., 2023; Wei et al., 2023; Haley et al., 2024; Mahapatra et al., 2024a; Costa Freitas et al., 2025; Feres et al., 2025; Kawahala et al., 2025; Pacakova et al., 2025). Phyllosilicates are naturally occurring LMs with a large band gap energy, making them suitable as dielectrics in ultrathin van der Waals heterostructures (vdWHs) (Barcelos et al., 2018; Janica et al., 2018; Gadelha et al., 2021; Nutting et al., 2021; Prando et al., 2021; Vasic et al., 2021; Barbosa et al., 2025). Moreover, defects and impurities in this material class allow free charges on the material surface to be transferred to another LM, modifying the overall optical and electrical properties of the 2DM-based devices (Mania et al., 2017; Mahapatra et al., 2022, 2023; de Oliveira et al., 2024a; Pramanik et al., 2024; Ames et al., 2025). Phyllosilicates are Earth-abundant minerals, easy to extract, easily handled, and air-stable, with the common presence of iron (Fe) impurities, from which magnetic proximity effects and magnetic properties can arise, even at the monolayer limit (Matković et al., 2021; Khan et al., 2023; Mahapatra et al., 2024b; Pacakova et al., 2025).

Biotite emerges as a phyllosilicate of interest within the framework of Earth-abundant insulating LM sources, due to the possibility of tuning its optical and magnetic properties by controlling the Fe content. Also known as black mica, biotite is a phyllosilicate within the trioctahedral mica group with the chemical formula K(Mg,Fe)₃AlSi₃O₁₀(OH)₂ (Deer and Howie, 1962; Maslova et al., 2004; Deer et al., 2013) (see Figs. 1ac). Moreover, biotite forms a solid-solution series with the phyllosilicate phlogopite ($KMg_3(AlSi_3)O_{10}(OH)_2$), which is a Fe-free phyllosilicate in principle, and annite ($KFe_3AlSi_3O_{10}(OH)_2$), the ideal Fe-endmember (Deer and Howie, 1962). The general lamellar structure of biotites (Fig. 1c) is oriented along the c-axis formed by the intercalation of two tetrahedral silicon oxide layers (T), with one Al-for-Si substitution, with (Mg,Fe)-trioctahedral layers (Oc) and K between the layers (Deer and Howie, 1962; Frisenda et al., 2020), forming a T-Oc-T structure with a cationic interlayer. The Oc layer has three possible sites, two of which are equivalent and called M1(B) sites, in which the six-coordinated ions are surrounded by four O and two OH in a cis-configuration (RausellColom et al., 1979). The non-equivalent site is in a *trans*-configuration, called M1(A) site (Rausell-Colom et al., 1979). Fe atoms are expected to be present in biotites in different valence states $Fe^{2+/3+}$ in the octahedral sites. The typical M1(A)-O atomic distances are smaller than the M1(B)-O distances. Thus, ions with smaller ionic radius, such as Fe^{3+} ions, tend to occupy the M1(A) sites, while Fe^{2+} ions tend to occupy M1(B) sites, typically with twice the abundance. However, the Fe-end member of the phlogopite-annite series is expected to have only Fe^{2+} ions occupying all octahedral sites. Furthermore, Fe^{3+} ions can also occupy the Altetrahedral sites (Tripathi et al., 1978; Rausell-Colom et al., 1979; Rancourt et al., 1992).

This work provides a fresh understanding of the physical properties of bulk biotites in relation to their Fe content in different oxidation states, using a correlative approach to serve as a robust reference for studies exploring few-layer biotites embedded in vdWHs and ultrathin devices. The present work investigates the structural, optical, and magnetic properties of biotite crystals to improve the understanding of how Fe concentration and oxidation state influence these properties. Due to the natural origin of the minerals studied in this work, structural defects or minor contributions from trace elements may also partially influence their fundamental properties. However, the focus was placed on the major contributions resulting from differences in iron content. An extensive correlative study was carried out on two biotite samples with phlogopite-like and annite-like behaviors using several experimental techniques. Finally, the use of these crystals as substrates for vdWHs incorporating monolayer (ML) MoSe2 is explored by magneto photoluminescence (PL) at cryogenic temperatures. These findings suggest biotite as a promising LM for developing low-cost magneto-optical and vdWHs-based devices due to its environmental stability and natural abundance.

2. Materials and methods

This work investigates two geological biotite specimens obtained from locations in Brazil and England to understand compositional variations in naturally occurring biotite. Since biotite forms a solid-solution series spanning a wide range of Fe contents, two samples were selected: the Brazilian specimen, mineralogically closest to phlogopite (the Fefree endmember), and the English specimen, closest to annite (the Feendmember). For clarity, they are referred to as phlogopite-like and

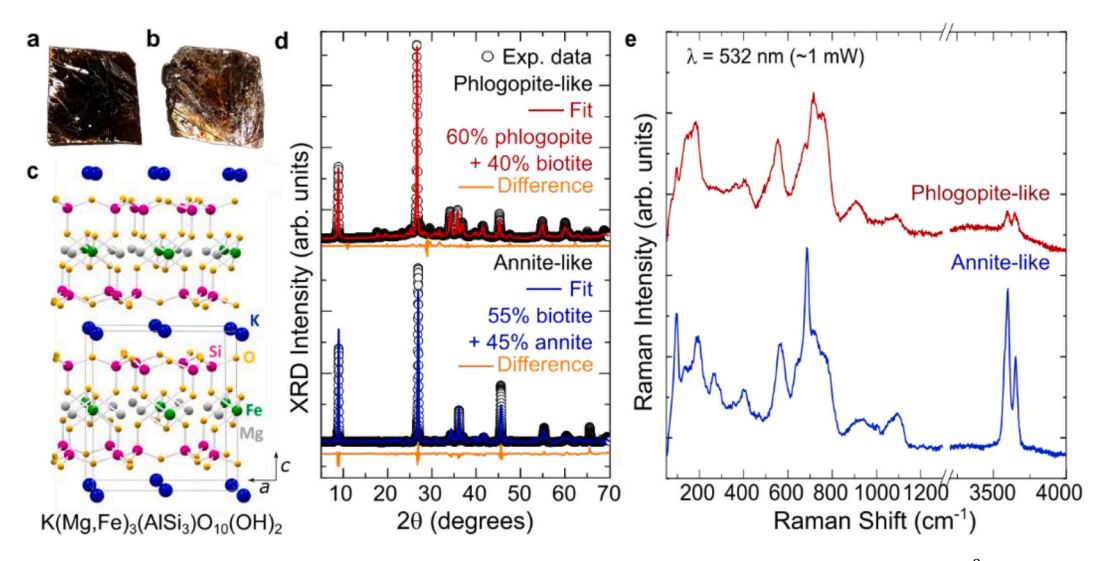


Fig. 1. Mineralogical characterization. a) Phlogopite-like and b) annite-like natural crystals with dimensions of $\sim 5 \times 5 \times 1$ mm³. c) Atomic structure of Fe-rich biotites with general chemical formula $K(Mg,Fe)_3(AlSi_3)O_{10}(OH)_2$. d) XRD measurements (black circles) for phlogopite-like (top) and annite-like (bottom) samples fitted through Rietveld refinement considering contributions of phlogopite and biotite mineralogical phases for phlogopite-like sample (red) and biotite and annite-like phases for annite-like sample (blue), along with their difference (orange) from the experimental data. e) Raman spectra of phlogopite-like (red) and annite-like (blue) samples. (For interpretation of the references to colour in this figure legend, the reader is referred to the web version of this article.)

annite-like samples, respectively.

2.1. Mineralogical characterization

X-ray diffraction (XRD) patterns were recorded in a Rigaku Miniflex II system with Cu-K α radiation ($\lambda=1.5418$ Å), employing a four-crystal Ge (220) (4-bounce) monochromator. The sample is measured in a two-axis diffractometer (operated in vertical geometry, in the Bragg–Brentano (θ :20) condition), using a NaI scintillator detector. The source divergence with this optical setup is nominally 1 mrad, and both receiving and anti-scatter slits were set to the minimum value of 0.625° . The generator was operated with a voltage and current of 30 kV and 15 mA, respectively.

Raman spectra were acquired using a Horiba XploRATM plus system with a 532 nm laser at 1 mW power. Spectra were accumulated 3 times for 30 s each, using a 1200 grooves/mm grating. Measurements employed a 100× objective (numerical aperture of 0.9), and the system was calibrated against the silicon peak at 521 cm $^{-1}$. Data were collected from $\sim\!1~\mu m$ diameter areas on mechanically exfoliated, bulk-like flat flakes transferred to silicon wafers.

2.2. Iron-content characterization

Energy-Dispersive Spectroscopy (EDS) was performed using a Thermo Scientific Helios 5 PFIB CXe DualBeam scanning electron microscope at an accelerating voltage of 15 kV and a current of 0.2 nA, in secondary electron imaging mode, with a chamber vacuum of 4.74 \times 10^{-5} Pa and an estimated spot size below 1 μm . Measurements were made on bulk biotite crystals ($\sim \! 5 \times 5 \text{ mm}^2$ area) after the cleavage of superficial layers using mechanical exfoliation. The samples were glued using carbon tape in an aluminum sample holder. The EDS calibration was performed using a standard 100 % silver (Ag) sample, resulting in a measurement error of approximately 2 %. Multiple points were analyzed for statistical representation; data from a representative location reflecting average composition were selected, excluding anomalous regions.

Absorbance and the reflectance spectra for Tauc plot analysis obtained using a Shimadzu 3600 Plus Ultraviolet–Visible–Near-Infrared (UV–Vis-NIR) spectrometer with 5.0 nm slit width. Measurements were conducted on bulk biotite crystals peeled off from the bulk crystals with homogeneous thickness ($\sim\!5\times5$ mm 2 area) and fixed to the sample holder.

X-ray fluorescence (XRF) hyperspectral maps of exfoliated biotite on Kapton tape were acquired at the CARNAUBA beamline (Tolentino et al., 2021) using synchrotron radiation over a $50\times50~\mu m^2$ area with $500\times500~nm^2$ pixel resolution. The X-ray beam spot measured $500\times200~nm^2$, with data collected in air at 9.75 keV excitation energy. Fe-K α emission was selected for image generation. X-ray absorption near edge structure (XANES) spectra around the Fe-K edge were recorded in fluorescence mode at about 300 K. Standard references for Fe oxidation states (metallic Fe – Fe 0 , FeO – Fe 2 +, Fe $_2$ O $_3$ – Fe 3 +, and Fe $_3$ O $_4$ – mixed Fe 2 +, Fe 3 +) were used for calibration and analyzed with Athena software (Ravel and Newville, 2005).

2.3. Optical and magneto-optical characterization

Photoluminescence (PL) measurements were performed in a custom setup optimized for the UV–visible range, featuring a Shamrock 500i spectrograph coupled with a CCD DU420A-BU detector and a continuous-wave 360 nm laser (CNI Model: UV-FN-360) at 1 mW. The estimated laser spot size on the sample is $\sim\!\!50~\mu m$. For room-temperature measurements, bulk flat biotite fragments with $\sim\!\!5\times5~mm^2$ peeled from the bulk biotite crystals were mounted inside a closed-cycle Janis CCS-150 cryostat in vacuum (5 \times 10 $^{-6}$ mbar).

Magneto-optical measurements were performed in a helium closedcycle cryostat equipped with superconducting magnet coils (Attocube Attodry1000) and magnetic fields (B) of up to 9 T at 3.6 K. The vdWH samples were mounted on Attocube piezoelectric xyz translation stages to control the sample position. μ -PL measurements were performed using a continuous wave laser with a photon energy of 1.88 eV and 100 μ W laser power with an estimated laser spot size on the sample of \sim 1 μ m. The PL signal was collimated using an Attocube aspheric lens (NA = 0.64). The selection of circular polarization components (σ + and σ -) was performed by using a linear polarizer and a quarter-wave plate before being focused into a 50 μ m multimode optical fiber. The PL signal was then dispersed by a 75 cm Andor spectrometer and detected by a silicon CCD detector (Andor, Shamrock/iDus). Details can be found in Toledo et al., (Roberto de Toledo et al., 2025).

2.4. Magnetic characterization

The magnetic properties of the phlogopite-like and annite-like biotite samples were investigated using a superconducting quantum interference device (SQUID) magnetometer (MPMS3, Quantum Design). Samples were prepared by cleaving a small fragment ($\sim 3 \times 3 \text{ mm}^2$) from the bulk biotite crystals, and their masses were subsequently measured. Magnetization (M) measurements were conducted at 300 K and 2 K. with magnetic fields up to 20 kOe applied parallel to the sample surface. Additionally, temperature-dependent magnetization, M(T), was measured under zero-field-cooled (ZFC) and field-cooled (FC) protocols, using an applied magnetic field of 100 Oe. In the ZFC protocol, the samples were cooled down from 300 K to 2 K in zero-field. Once the temperature stabilized at 2 K, a magnetic field was applied, and data were collected during warming at a rate of 0.1 K/min. For the FC protocol, the samples were cooled under the applied field, and data were collected during cooling down. The temperature derivative of magnetization (dM/dT) was calculated to identify possible magnetic transitions.

2.5. Van der Waals heterostructures stacking

vdWHs composed of ML-MoSe $_2$ and phlogopite/annite-like flakes were prepared on SiO_2/Si substrates by mechanical exfoliation and the dry-transfer process technique. The ML-MoSe $_2$ flakes were obtained from the exfoliation of the MoSe $_2$ -bulk crystal (2D Semiconductors) onto a polydimethylsiloxane (PDMS) stamp by the scotch tape technique and selected under an optical microscope (Castellanos-Gomez et al., 2014). The ML-MoSe $_2$ /PDMS stamps were then aligned and stamped on the phlogopite (or annite)-like flakes slabs using a commercial transfer system (HQ Graphene).

3. Results and discussion

To investigate the structural properties of the biotite samples, XRD measurements were performed on freshly milled mineral powders (Fig. 1d). For Rietveld refinement of the diffractograms, biotite (Brigatti and Davoli, 1990), phlogopite (Hendricks and Jefferson, 1939), and annite (Redhammer et al., 2000) were considered as the main phases. The experimental data were fitted using the MAUD software package (Lutterotti et al., 1997), yielding good agreement with respect to peak intensities and positions, as indicated by the difference plot (orange line) between the fit and the experimental data for each sample. The most common biotite polytype exhibits monoclinic symmetry with a C2/m space group (Ross et al., 1966). For the phlogopite-like powder, the best fit was obtained with a volumetric combination of 40 % biotite and 60 %phlogopite phases. In contrast, for the annite-like powder, the best fit required a volumetric combination of 55 % biotite and 45 % annite phases. The structural parameters derived from the XRD fitting are summarized in Table 1. These results indicate that, although both samples are biotite minerals, the incorporation of Fe significantly affects the phase composition. In the phlogopite-like sample, whose diffractogram adjustment showed a dominant phlogopite contribution and a

Table 1
Crystal lattice parameters of phlogopite and annite-like biotites retrieved from Rietveld refinement

Biotite sample	phase	a (Å)	b (Å)	c (Å)	α = γ (°)	β (°)
phlogopite- like	biotite	5.367 (5)	9.266 (8)	10.196 (2)	90	100.12 (6)
	phlogopite	5.311 (1)	9.034 (1)	10.097 (2)	90	96.02 (2)
annite-like	biotite	5.367 (8)	9.228 (9)	10.04 (1)	90	101.8 (1)
	annite	5.391 (6)	9.335 (4)	10.308 (3)	90	100.4 (1)

minor biotite contribution (red line), Mg is expected to be more abundant than Fe in the octahedral sites. On the other hand, the diffractogram of the annite-like sample could not be accurately fitted using only the biotite phase. An almost equal contribution from biotite and annite (blue line) was required, suggesting that Fe occupies a larger fraction of the octahedral sites compared to Mg in this sample. As will be discussed later, the Fe ions occupying the octahedral sites in the annite-like sample are predominantly in the ${\rm Fe}^{2+}$ oxidation state, consistent with annite's composition.

The Raman spectra of the samples are shown in Fig. 1e. Both the phlogopite-like and annite-like samples display twelve characteristic Raman modes at approximately 95, 140, 180, 405, 555, 680, 715, 760, 910, 1090, 3600, and 3650 ${\rm cm}^{-1}$, appearing as broadened peaks with unresolved shoulders. The peak positions are nearly identical between the two samples. This high degree of spectral correspondence indicates that the general vibrational modes are consistent with those of biotite and annite, despite the expected predominance of Fe²⁺-Oc sites for the

annite-like sample. The main differences observed in the Raman spectrum of the annite-like, when compared to the phlogopite-like one, include more intense and better-defined peaks in the 3500-3800 cm⁻¹ range, attributed to OH-stretching modes (Aspiotis et al., 2022), as well as a more intense mode at 680 cm⁻¹, in addition to two extra pronounced modes at 265 and 640 cm⁻¹. The spectra are in good agreement with previously reported Raman spectra of biotite (Loh, 1973; Sontevska et al., 2007; Singh and Singha, 2016; Ulian and Valdrè, 2023). The Oclayer vibrations dominate the spectrum up to 600 cm⁻¹, followed by T ring modes up to 800 cm⁻¹ and T-stretching modes up to 1200 cm⁻¹ (Aspiotis et al., 2022). The peaks corresponding to OH-stretching modes are highly sensitive to the chemical composition of the Oc sites (Wang et al., 2015; Aspiotis et al., 2022; Khan et al., 2023). In pure annite phases, only one OH-stretching peak is typically expected, resulting from the ordered occupation of Fe²⁺-Fe²⁺-Fe²⁺ in the Oc sites. However, the annite-like sample investigated here contains two main mineralogical phases, involving varying occupancies of Fe, Mg, and possibly Al as substitutional ions in the Oc sites. This compositional variation can lead to the splitting of OH-stretching peaks, as also discussed in reference (Aspiotis et al., 2022). In contrast, the phlogopite-like sample shows weaker OH-stretching features, consistent with a mixed contribution from less probable Oc configurations. This suggests that the phlogopitelike sample incorporates more Fe³⁺ than the annite-like one, enabling a greater variety of possible structural arrangements.

The chemical composition of the two samples was analyzed with particular focus on Fe incorporation. Representative EDS spectra for the phlogopite-like and annite-like samples are shown in Fig. 2a, normalized by the oxygen peak, which is the most intense. Based on the EDS data, the elemental composition of the samples can be qualitatively assessed. The spectra reveal the presence of aluminum (Al), potassium (K), magnesium (Mg), oxygen (O), and silicon (Si), and iron (Fe) as the main

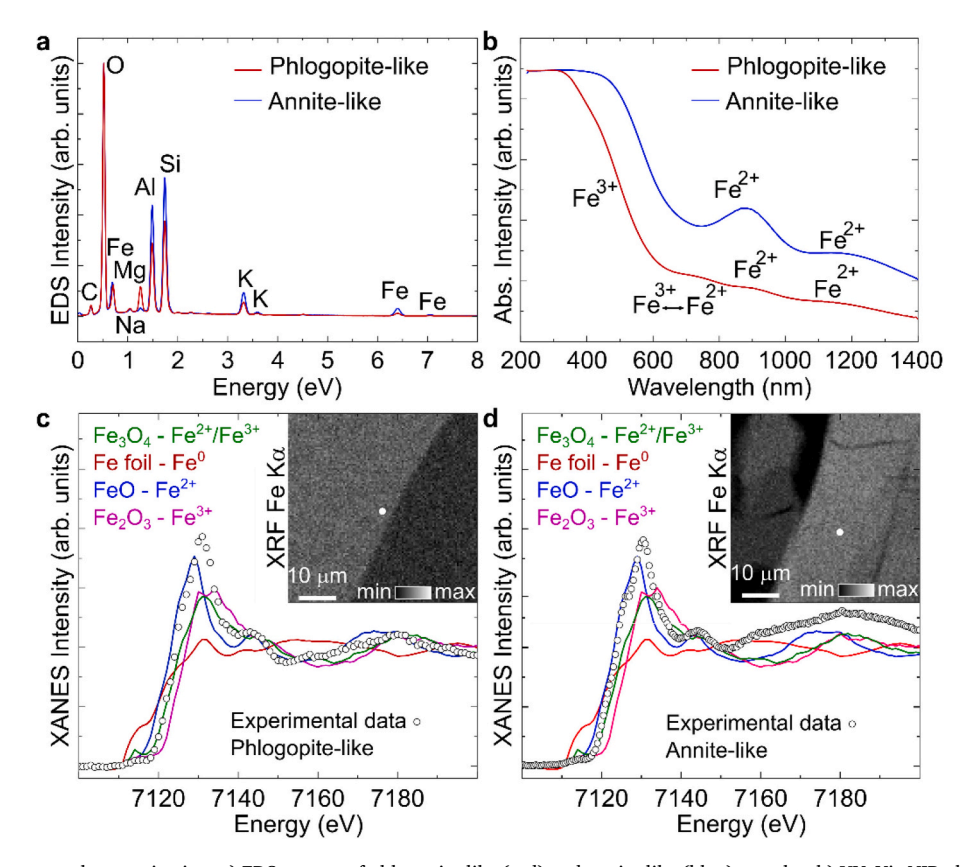


Fig. 2. Fe-content spectroscopy characterization. a) EDS spectra of phlogopite-like (red) and annite-like (blue) samples. b) UV-Vis-NIR absorbance spectra from the same samples. Fe K-edge XANES spectra collected at the location marked by a white dot in the corresponding XRF maps (insets) of c) phlogopite-like and d) annite-like samples, compared with reference iron oxides of known oxidation states. XRF mapping was performed with 500 nm spatial resolution at the Fe-K α emission energy. (For interpretation of the references to colour in this figure legend, the reader is referred to the web version of this article.)

constituent elements. No additional impurities were detected. The observed sodium (Na) and carbon (C) signals are attributed to sample handling and environmental exposure. The primary spectral difference between the samples lies in the lower Mg content observed in the annitelike sample compared to the phlogopite-like one, which is compensated by higher concentrations of Al and Fe. This result is consistent with the XRD quantification, which indicated ~45 % annite phase in the annitelike sample. Although EDS is a limited technique for quantitative analysis, it is possible to perform a semi-quantitative elemental analysis, taking care to choose a flat surface of freshly cleaved samples as representative regions, avoiding increasing error due to roughness and contamination. The semi-quantitative results are summarized in Table 2, presenting the concentrations of the main constituent elements (O, Si, Al, Fe, Mg, and K) from representative regions of each sample. The remaining detected content corresponds to Na and C. Our compositional analysis confirms that both phlogopite-like and annite-like samples exhibit major elemental concentrations in agreement with literature values (Zheng et al., 2020) (see Table 2). However, it is essential to note that the EDS has limited sensitivity for elements present at concentrations below ~2 wt%, which restricts the reliable quantification of trace

Now, to evaluate the oxidation states of iron in the biotite samples, spectroscopic characterizations were performed. UV–Vis-NIR absorption measurements, shown in Fig. 2b, revealed absorption bands associated with Fe $^{2+}$ and Fe $^{3+}$ valence states, as expected for phyllosilicate minerals (G. H. Faye, 1968). In the annite-like sample, the absorption band related to the Fe $^{2+}$ -Fe $^{3+}$ charge exchange is almost suppressed, while the Fe $^{2+}$ bands are much more pronounced than in the phlogopite-like sample. This suggests that the Oc layer in the annite-like sample is chemically well-defined by a dominant presence of Fe $^{2+}$ ions. These findings are consistent with the EDS and Raman spectroscopy results, which indicate a more chemically diverse Oc layer in the phlogopite-like sample.

To further investigate the iron oxidation states, advanced synchrotron-based spectroscopic techniques were employed on multilayer exfoliated flakes. Using an X-ray nanoprobe, XRF and XANES measurements were conducted to probe the spatial distribution and oxidation state of Fe with sub-micrometric resolution. XRF microscopy was performed over a 50 \times 50 μ m² area on both phlogopite-like and annite-like flakes. Hyperspectral maps (insets in Figs. 2c,d) were generated by selecting the spectral response around the Fe-K α emission energy, with a spatial resolution of $500 \times 500 \text{ nm}^2$ per pixel. Both samples exhibit a homogeneous Fe distribution, with XRF intensity modulated by thickness (i.e., brighter areas = thicker sample regions, while darker areas = thinner sample regions). XANES spectra were acquired at the location marked by the white dots in the insets of Figs. 2c,d, and analyzed qualitatively by comparing them with reference spectra of iron oxides with known oxidation states (Figs. 2c,d). The phlogopite-like sample exhibits a magnetite-like signature, with its Fe-edge aligning with that of the Fe₃O₄ (magnetite) standard, indicating a mixed Fe²⁺/ Fe³⁺ oxidation state. In contrast, the annite-like sample matches the absorption edge of the FeO standard, confirming the presence of iron predominantly in the Fe²⁺ state. These results agree with our UV-Vis-NIR absorbance analysis, while also providing enhanced spatial resolution and sensitivity. The synchrotron-based X-ray nanoprobe enables

Table 2Semi-quantitative analysis of phlogopite and annite-like biotites using EDS.

Element	phlogopite-like (wt%)	annite-like (wt%)	
0	57	50	
Si	15	18	
Al	11	13	
Fe	4	8	
Mg	4	1	
K	4	6	

the investigation of significantly smaller sample areas with sub-micrometric precision(Tolentino et al., 2023).

Next, the influence of Fe content on the optical properties of the samples was investigated. In particular, PL spectra were measured for both biotite crystals at various positions at 300 K, as shown in Figs. 3a-d. Overall, the PL spectra reveal different emission bands associated with optical transitions related to the presence of defects. For the biotite samples studied, these defects are mainly associated with Fe incorporation. Figs. 3a,b show typical PL spectra for both samples at 300 K. A broad, asymmetrical PL band centered ~2.8 eV is typically observed across most of the measurement positions. However, at certain locations, a stronger PL signal is detected with well-resolved emission bands, indicating multiple optical contributions (Figs. 3c,d). Deconvolution of the broad PL spectra by Voigt functions (represented by blue, green, purple, orange, and cyan areas) reveals the presence of four emission bands approximately 3.20, 3.00, 2.84, 2.71, and 2.65 eV for the phlogopite-like sample, and five bands at around 3.00, 2.84, 2.71, and 2.50 eV for the annite-like sample. The primary optical emissions from both samples are likely associated with transitions involving defect states with high energy, followed by relaxation processes resulting in lower-energy emissions. In general, the PL results are consistent with the reflectance data, and their origin is attributed to transitions related to Fe within the crystal structure.

To further investigate these transitions, UV-Vis-NIR reflectance measurements were carried out. For this, Tauc plots were derived from the reflectance spectra of the phlogopite-like (Fig. 3e) and annite-like (Fig. 3f) samples. The band gap energies were estimated by extrapolating the linear portions of the Kubelka-Munk function (Kubelka and Munk, 1931; Makuła et al., 2018). For the phlogopite-like sample, a nonlinear continuous trend is observed with increasing photon energy, suggesting a broad energy distribution of defect states. This behavior may arise from disordered defects caused by local site configuration variations or from defect band formation in regions with high defect concentration and long-range order. Both scenarios are plausible, given that biotite is inherently a solid solution with high Fe incorporation in various sites and oxidation states. Despite the continuous nature of the curve, three approximate linear regimes can be distinguished, corresponding to estimated optical transitions at 1.75(5) eV (blue line), 2.30 (5) eV (green line), and 2.80(5) eV (red line). In contrast, the annite-like sample exhibits two well-defined linear regimes, separated by a discontinuity around 3 eV in Fig. 3f. The first regime yields an optical transition at 1.90(5) eV (blue line). In the second regime, a further discontinuity is observed near 4 eV, and two linear fits (green and red lines) converge to the same estimated optical transition at 2.75(5) eV. These different estimated band gaps indicate the presence of distinct defect levels involved in the optical transitions of the samples, which is consistent with the various emission bands observed in the PL spectra of the biotite samples (Fig. 3).

The magnetic properties of both phlogopite-like and annite-like biotite samples were thoroughly investigated through M(H) and M(T) measurements (Fig. 4). The M(H) curves at 300 K and 2 K reveal a typical paramagnetic behavior for both samples, consistent with the presence of Fe in different oxidation states (Fe $^{2+}$ and Fe $^{3+}$) within the Oc layers (Fig. 4a,d). However, at 2 K, a small but noticeable hysteresis is observed, particularly in the phlogopite-like sample, suggesting the emergence of weak ferromagnetic interactions or spin-canting effects at low temperatures. This hysteresis is less pronounced in the annite-like sample, indicating a possible dependence of magnetic behavior on the Fe content and its distribution within the crystal lattice.

The M(T) measurements further elucidate the magnetic properties of the samples (Fig. 4b,e). A distinct transition is observed in the ZFC curves, and the critical ordering temperatures were identified by analyzing the temperature derivative of magnetization (dM/dT) from the FC measurements. For the annite-like sample, the transition occurs at 2.6 K (Fig. 4c), whereas the phlogopite-like sample exhibits a transition at a slightly higher temperature of 4 K (Fig. 4f). These transitions

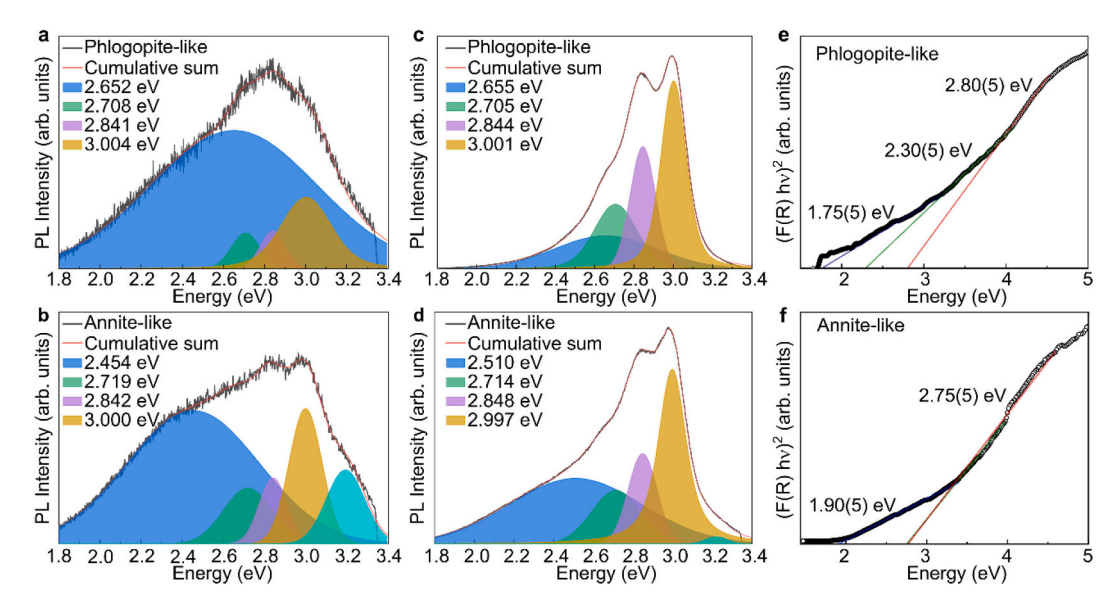


Fig. 3. Optical properties of biotite samples. PL spectra acquired at 300 K for a) phlogopite-like and b) annite-like samples. PL obtained for measurement positions with stronger PL intensity for c) phlogopite-like and d) annite-like positions. The red lines are the cumulative sum of the individual emission peaks deconvolved in the blue, green, purple, orange, and cyan areas. Tauc plot obtained from UV–Vis-NIR reflectance measurements for e) phlogopite-like and f) annite-like samples showing the estimation of defect optical transitions (blue, green, and red lines). (For interpretation of the references to colour in this figure legend, the reader is referred to the web version of this article.)

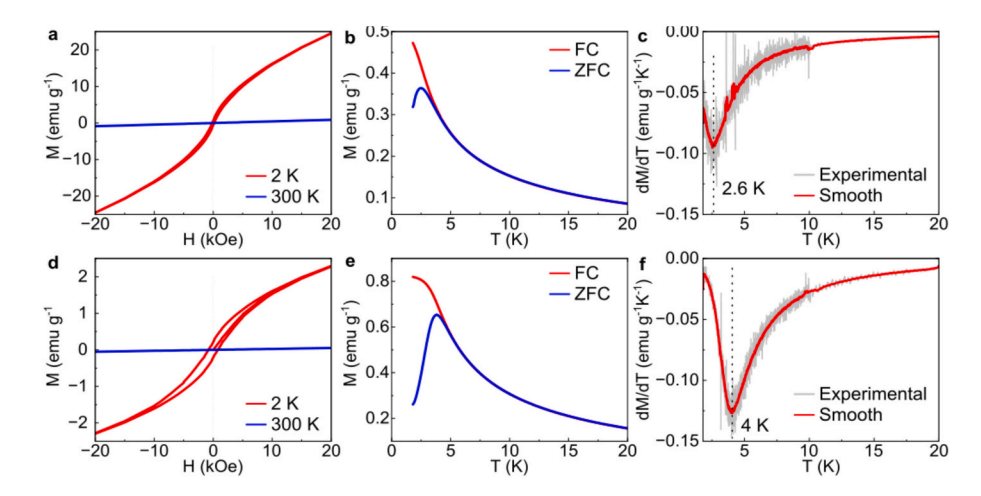


Fig. 4. Magnetic characterization of biotite samples. a-c) Annite-like sample: a) M(H) hysteresis loop, b) FC-ZFC M(T) curve, and c) temperature derivative of magnetization (dM/dT) from FC measurements. d-f) Phlogopite-like sample: d) M(H) hysteresis loop, e) FC-ZFC M(T) curve, and f) dM/dT from FC measurements. All measurements were conducted with the magnetic field applied parallel to the sample surface, and the M(T) measurements were carried out under an applied magnetic field of 100 Oe.

may be attributed to spin freezing or the onset of short-range magnetic order, influenced by the differing iron concentrations and oxidation states in the two samples. The FC curves diverge from the ZFC curves below the transition temperatures, indicating magnetic irreversibility and the presence of competing magnetic interactions.

The observed differences in magnetic behavior between the two samples correlate with their structural and compositional characteristics, as revealed by XRD, EDS, XANES, Raman, and UV–Vis-NIR spectroscopy. The higher transition temperature and more prominent hysteresis in the phlogopite-like sample suggest a stronger influence of Fe³⁺ ions, which may occupy specific Oc sites and contribute to localized magnetic moments. In contrast, the annite-like sample, with a higher Fe²⁺ content, shows a lower transition temperature, reflecting distinct magnetic interactions associated with Fe²⁺-dominated environments. These results are consistent with previous studies (Beausoleil et al., 1983; Khan et al., 2023), which indicate that a small fraction of

 $\rm Fe^{3+}$ enhances ferromagnetic interactions when it is surrounded only by $\rm Fe^{2+}$ ions. However, as the $\rm Fe^{3+}$ concentration increases, the formation of $\rm Fe^{3+}$ -Fe^{3+} pairs becomes more likely, leading to dominant antiferromagnetic interactions. Thus, the present study provides experimental confirmation, demonstrating that although the total iron concentration significantly influences the mineral's properties, it is the $\rm Fe^{3+}/\rm Fe^{2+}$ ratio that serves as the key parameter for tuning its magnetic behavior. This finding may also be relevant for flakes with few-layer thicknesses and could be extended to explain recent results on vermiculite crystals (Pacakova et al., 2025).

Finally, the use of these crystals with different iron concentrations and oxidation states as ultrathin substrates for ML-MoSe $_2$ is explored. To this end, magneto-PL measurements were performed on ML-MoSe $_2$ /phlogopite(annite)-like heterostructures (Fig. 5a,b) assembled onto SiO $_2$ /Si substrates under out-of-plane magnetic field. Fig. 5a,b shows the typical σ^+ and σ^- PL spectra recorded at 9 T and 3.6 K. In these spectra,

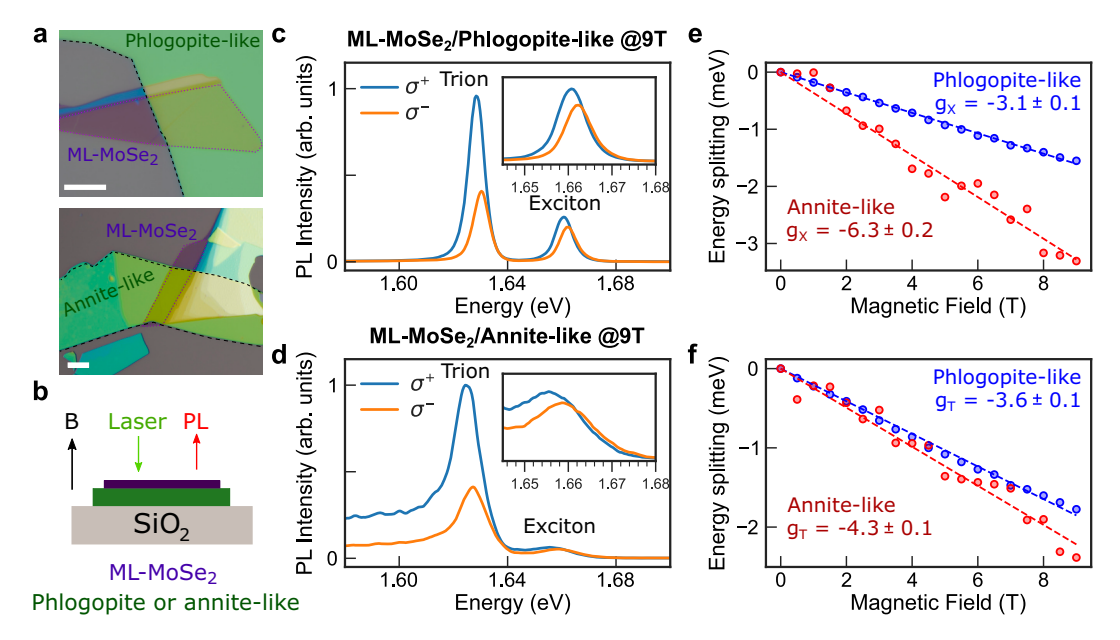


Fig. 5. a) Optical microscope images of ML-MoSe $_2$ onto a phlogopite-like and annite-like flakes, assembled onto SiO $_2$ /Si substrate. b) Schematic drawing of a vdWHs under an out-of-plane magnetic field. c,d) Circularly polarization resolved PL spectra (σ + and σ -) for ML-MoSe $_2$ /phlogopite-like and ML-MoSe $_2$ /annite-like vdWHs, respectively, under out-of-plane magnetic fields at 3.6 K. e,f) Energy splitting as a function of magnetic field for the exciton (X) and trion (T) emission peaks in ML-MoSe $_2$ /phlogopite-like and ML-MoSe $_2$ /annite-like vdWHs, respectively. The laser excitation is linearly polarized, and the PL detection is circularly polarized (σ + and σ -).

two distinct PL peaks are observed, corresponding to exciton (X) and trion (T) emissions (Glazov et al., 2024). Fig. 5c,d present the Zeeman splitting (ΔE), fitted using $\Delta E = E^{\sigma+} - E^{\sigma-} = g \, \mu_B B$, where $\mu_B = 58 \, \mu eV/T$ is the Bohr magneton, B is the out-plane magnetic field, and g is the valley g-factor. $E^{\sigma+}$ and $E^{\sigma-}$ represent the PL peak energies of the $\sigma+$ or $\sigma-$ components for either the T or X emissions (de Oliveira et al., 2024a; Glazov et al., 2024).

The extracted X g-factor values are approximately -6.3 and -3.1 for the ML-MoSe₂ on annite- and phlogopite-like slabs, respectively. These results indicate a significant enhancement of the X g-factor for the ML-MoSe₂ on the annite-like flake, whereas a notable reduction is observed on the phlogopite-like substrate. The obtained g-factor values deviate considerably from typical values reported in literature, which generally range from -3.8 to -4.2 (Woźniak et al., 2020; Covre et al., 2022; Faria Junior et al., 2022; Gobato et al., 2022). This deviation is attributed to the presence of local iron impurities with varying oxidation states. The ML-MoSe₂ flake can hybridize with the underlying annite- and phlogopite-like layers, which may contain magnetic impurities at the interface (de Oliveira et al., 2024a). This hybridization could influence the valley properties of ML-MoSe₂. Furthermore, the extracted T g-factor values are approximately -4.3 and -3.6 for ML-MoSe2 on annite- and phlogopite-like flakes, respectively. Interestingly, these values show only slight variations compared to those reported in the literature, suggesting that iron impurities predominantly affect the X g-factors rather than the T g-factors in ML-MoSe₂/biotite heterostructures, which is an unusual and intriguing result. Therefore, further studies are necessary to understand in detail the impact of iron impurities on the valley properties of ML-MoSe₂/phlogopite(annite)-like vdWHs.

4. Conclusion

This work presents a comprehensive investigation of the structural, optical, and magnetic properties of two naturally occurring biotite samples with distinct iron contents and oxidation states. By employing a combination of advanced characterization techniques, including XRD, Raman spectroscopy, EDS, UV–Vis-NIR, XANES, PL, and SQUID magnetometry, we demonstrate that the Fe content and its valence state significantly influence the material's optical transitions and magnetic

behavior. The phlogopite-like sample, richer in ${\rm Fe}^{3+}$, shows enhanced magnetic ordering and broader optical transitions. In contrast, the annite-like sample, dominated by ${\rm Fe}^{2+}$, exhibits more defined structural features and lower-temperature magnetic transitions. These findings establish a clear correlation between iron incorporation and the fundamental physical properties of biotite, providing critical insights for its use in future van der Waals heterostructures and magneto-optical devices.

In addition, it has been investigated the impact of using biotite crystals with different iron concentrations and oxidation states as magnetic substrates for MoSe₂ monolayers. The magneto-PL results show that the presence of iron impurities with varying oxidation states has a significant impact on the valley properties for ML-MoSe₂. In particular, it was observed unusual variations in the exciton g-factor values of ML-MoSe₂/phlogopite (annite)-like heterostructures. Furthermore, by providing experimental benchmarks on the oxidation states, atomic occupancy, and defect-sensitive properties of biotite, this work may serve as a valuable reference for theoretical studies. It can inspire first-principles simulations focused on the energetic stability of Fe ions in distinct lattice sites and oxidation states, as well as the role of defects and impurities in tuning the material's electronic and magnetic behavior at the atomic scale.

CRediT authorship contribution statement

Raphaela de Oliveira: Writing – review & editing, Writing – original draft, Methodology, Formal analysis, Data curation. Yara Galvão Gobato: Writing – review & editing, Writing – original draft, Funding acquisition, Formal analysis. Ronei C. de Oliveira: Writing – review & editing, Formal analysis, Data curation. José R. de Toledo: Writing – review & editing, Investigation, Data curation. Verônica C. Teixeira: Writing – review & editing, Investigation, Formal analysis. Angelo Malachias: Writing – review & editing, Writing – original draft, Formal analysis, Data curation. Cesar R. Rabahi: Methodology, Investigation. Chunwei Hsu: Investigation. Adilson J.A. de Oliveira: Writing – review & editing, Writing – original draft, Funding acquisition, Formal analysis. Herre S.J. van der Zant: Writing – review & editing, Investigation. Ingrid D. Barcelos: Writing – review & editing, Visualization,

Funding acquisition. **Alisson R. Cadore:** Writing – review & editing, Writing – original draft, Supervision, Investigation, Conceptualization.

Declaration of competing interest

The authors declare that they have no known competing financial interests or personal relationships that could have appeared to influence the work reported in this paper.

Acknowledgments

All Brazilian authors thank the financial support from "Fundação Coordenação de Aperfeiçoamento de Pessoal de Nível Superior" (CAPES), "Conselho Nacional de Desenvolvimento Científico e Tecnológico" (CNPq), "Fundação de Amparo à Pesquisa do Estado de Minas Gerais" (FAPEMIG). The authors thank the LNNano (Proposals: FTO-20221810. DRX-20230142. Raman-20230143. MNF-20230017. and MNF-20240039) and the Microscopic Samples Laboratory (LAM, at the LNLS - Proposals: LAM-2D-20230170, LAM-2D-20230164 and LAM-PFIB-20242188), and the CARNAUBA beamline at LNLS (Proposal: 20222162) both part of the CNPEM, a private nonprofit organization under the supervision of the Brazilian Ministry for Science, Technology, and Innovations (MCTI), for sample fabrication and characterization. This work was supported by "Fundação de Amparo à Pesquisa do Estado de São Paulo" (FAPESP) (grant numbers 21/10293-1, 22/00419-0, 22/ 08329-0, 23/11265-7, and 23/01313-4), and through the Research, Innovation and Dissemination Center for Molecular Engineering for Advanced Materials - CEMol (Grant CEPID No. 2024/00989-7), and Financiadora de Estudos e Projetos (FINEP) (grant 01.22.0178.00 -MATSemBGL (14796)). Finally, all authors thank Professor Marco A. Fonseca from Federal University of Ouro Preto for supplying the phlogopite-like biotite crystal, Dr. Jessica Fonsaca for enlightening discussion, and Carolina Torres, Cilene Labre, and Karen Bedin for experimental assistance.

Data availability

Data will be made available on request.

References

- Ames, A., Sousa, F.B., Souza, G.A.D., de Oliveira, R., Silva, I.R.F., Rodrigues, G.L., Watanabe, K., Taniguchi, T., Marques, G.E., Barcelos, I.D., Cadore, A.R., Lopez-Richard, V., Teodoro, M.D., 2025. Optical memory in a MoSe2/Clinochlore device. ACS Appl. Mater. Interfaces 17, 12818–12826. https://doi.org/10.1021/acsami.4c19337.
- Aspiotis, S., Schlüter, J., Redhammer, G.J., Mihailova, B., 2022. Non-destructive determination of the biotite crystal chemistry using Raman spectroscopy: how far we can go? Eur. J. Mineral. 34, 573–590. https://doi.org/10.5194/ejm-34-573-2022.
- Barbosa, T.C., Chaves, A.J., Freitas, R.O., Campos, L.C., Barcelos, I.D., 2025. Ultraconfined plasmons reveal moiré patterns in a twisted bilayer graphene-talc heterostructure. Nanoscale 17, 9205–9212. https://doi.org/10.1039/D4NR04532G.
- Barcelos, I.D., Cadore, A.R., Alencar, A.B., Maia, F.C.B., Mania, E., Oliveira, R.F., Bufon, C.C.B., Malachias, A., Freitas, R.O., Moreira, R.L., Chacham, H., 2018. Infrared fingerprints of natural 2D Talc and Plasmon–Phonon coupling in Graphene–Talc Heterostructures. ACS Photonics 5, 1912–1918. https://doi.org/ 10.1021/acsphotonics.7b01017.
- Barcelos, I.D., de Oliveira, R., Schleder, G.R., Matos, M.J.S., Longuinhos, R., Ribeiro-Soares, J., Barboza, A.P.M., Prado, M.C., Pinto, E.S., Gobato, Y.G., Chacham, H., Neves, B.R.A., Cadore, A.R., 2023. Phyllosilicates as earth-abundant layered materials for electronics and optoelectronics: prospects and challenges in their ultrathin limit. J. Appl. Phys. 134, 090902. https://doi.org/10.1063/5.0161736.
- Beausoleil, N., Lavallée, P., Yelon, A., Ballet, O., Coey, J.M.D., 1983. Magnetic properties of biotite micas. J. Appl. Phys. 54, 906–915. https://doi.org/10.1063/1.332053.
 Brigatti, M.F., Davoli, P., 1990. Crystal-structure refinements of 1M plutonic biotites. Am. Mineral. 75, 305–313.
- Cadore, A.R., de Oliveira, R., Longuinhos, R., Teixeira, V.C., Nagaoka, D.A., Alvarenga, V.T., Ribeiro-Soares, J., Watanabe, K., Taniguchi, T., Paniago, R.M., Malachias, A., Krambrock, K., Barcelos, I.D., de Matos, C.J.S., 2022. Exploring the structural and optoelectronic properties of natural insulating phlogopite in van der Waals heterostructures. 2d Mater. 9, 035007. https://doi.org/10.1088/2053-1583/ ac6cf4.

- Castellanos-Gomez, A., Buscema, M., Molenaar, R., Singh, V., Janssen, L., van der Zant, H.S.J., Steele, G.A., 2014. Deterministic transfer of two-dimensional materials by all-dry viscoelastic stamping. 2d Mater. 1, 011002. https://doi.org/10.1088/ 2053-1583/1/1/011002.
- Choi, W., Choudhary, N., Han, G.H., Park, J., Akinwande, D., Lee, Y.H., 2017. Recent development of two-dimensional transition metal dichalcogenides and their applications. Mater. Today 20, 116–130. https://doi.org/10.1016/j. mattod.2016.10.002.
- Costa Freitas, L.V., Rodrigues-Junior, G., Bernardes Marçal, L.A., Calligaris, G.A., Barcelos, I.D., de Oliveira, R., Malachias, A., 2025. Comparative study of phyllosilicate surface and sub-surface interlamellar water adsorption through crystal truncation rod modelling. Appl. Surf. Sci. 682, 161775. https://doi.org/10.1016/j. apsusc.2024.161775.
- Covre, F.S., Faria, P.E., Gordo, V.O., de Brito, C.S., Zhumagulov, Y.V., Teodoro, M.D., Couto, O.D.D., Misoguti, L., Pratavieira, S., Andrade, M.B., Christianen, P.C.M., Fabian, J., Withers, F., Galvão Gobato, Y., 2022. Revealing the impact of strain in the optical properties of bubbles in monolayer MoSe2. Nanoscale 14, 5758–5768. https://doi.org/10.1039/D2NR00315E.
- Craco, L., Carara, S.S., Chagas, E.F., Cadore, A.R., Leoni, S., 2025. Electronic correlation and Mott localization of paramagnetic CrSBr crystal. Eur. Phys. J. B. 98, 145. https://doi.org/10.1140/epjb/s10051-025-00991-6.
- Culcer, D., Cem Keser, A., Li, Y., Tkachov, G., 2020. Transport in two-dimensional topological materials: recent developments in experiment and theory. 2d Mater. 7, 022007. https://doi.org/10.1088/2053-1583/ab6ff7.
- de Oliveira, R., Cadore, A.R., Freitas, R.O., Barcelos, I.D., 2023. Review on infrared nanospectroscopy of natural 2D phyllosilicates. J. Opt. Soc. Am. A 40, C157–C168. https://doi.org/10.1364/JOSAA.482518.
- de Oliveira, R., Barbosa Yoshida, A.B., Rabahi, C.R., O Freitas, R., Teixeira, V.C., de Matos, C.J.S., Galvão Gobato, Y., Barcelos, I.D., Cadore, A.R., 2024a. Ultrathin natural biotite crystals as a dielectric layer for van der Waals heterostructure applications. Nanotechnology 35, 505703. https://doi.org/10.1088/1361-6528/ ad7b3a.
- de Oliveira, R., Freitas, L.V.C., Chacham, H., Freitas, R.O., Moreira, R.L., Chen, H., Hammarberg, S., Wallentin, J., Rodrigues-Junior, G., Marçal, L.A.B., Calligaris, G.A., Cadore, A.R., Krambrock, K., Barcelos, I.D., Malachias, A., 2024b. Water nanochannels in Ultrathin Clinochlore Phyllosilicate mineral with ice-like behavior. J. Phys. Chem. C 128, 14388–14398. https://doi.org/10.1021/acs.jpcc.4c02170.
- Deer, W.A., Howie, R.A., 1962. Rock Forming Minerals: Sheet Silicates, 3rd ed. Longmans. London.
- Deer, W.A., Howie, R.A., Zussman, J., 2013. An Introduction to the Rock-Forming Minerals. Mineralogical Society of Great Britain and Ireland. https://doi.org/ 10.1180/DHZ.
- Duan, Xidong, Wang, C., Pan, A., Yu, R., Duan, Xiangfeng, 2015. Two-dimensional transition metal dichalcogenides as atomically thin semiconductors: opportunities and challenges. Chem. Soc. Rev. 44, 8859–8876. https://doi.org/10.1039/ C5CS00507H.
- Faria Junior, P.E., Zollner, K., Woźniak, T., Kurpas, M., Gmitra, M., Fabian, J., 2022. First-principles insights into the spin-valley physics of strained transition metal dichalcogenides monolayers. New J. Phys. 24, 083004. https://doi.org/10.1088/ 1367-2630/ac7e21.
- Faye, G.H., 1968. The optical absorption spectra of iron in six-coordinate sites in chlorite, biotite, phlogopite and vivianite; some aspects of pleochroism in the sheet silicates. Can. Mineral. 9, 403–425.
- Feres, F.H., Maia, F.C.B., Chen, S., Mayer, R.A., Obst, M., Hatem, O., Wehmeier, L., Nörenberg, T., Queiroz, M.S., Mazzotti, V., Klopf, J.M., Kehr, S.C., Eng, L.M., Cadore, A.R., Hillenbrand, R., Freitas, R.O., Barcelos, I.D., 2025. Two-Dimensional Talc as a Natural Hyperbolic Material.
- Fiori, G., Bonaccorso, F., Iannaccone, G., Palacios, T., Neumaier, D., Seabaugh, A., Banerjee, S.K., Colombo, L., 2014. Electronics based on two-dimensional materials. Nat. Nanotechnol. 9, 768–779. https://doi.org/10.1038/nnano.2014.207.
- Frisenda, R., Niu, Y., Gant, P., Muñoz, M., Castellanos-Gomez, A., 2020. Naturally occurring van der Waals materials. NPJ 2D Mater. Appl. 4, 1–13. https://doi.org/
- Gadelha, A.C., Vasconcelos, T.L., Cançado, L.G., Jorio, A., 2021. Nano-optical Imaging of In-Plane Homojunctions in Graphene and MoS 2 van der Waals Heterostructures on Talc and SiO 2. J. Phys. Chem. Lett. 12, 7625–7631. https://doi.org/10.1021/acs. jpclett.1c01804.
- Glazov, M., Arora, A., Chaves, A., Gobato, Y.G., 2024. Excitons in two-dimensional materials and heterostructures: Optical and magneto-optical properties. MRS Bull. 49, 899–913. https://doi.org/10.1557/s43577-024-00754-1.
- Gobato, Y.G., de Brito, C.S., Chaves, A., Prosnikov, M.A., Woźniak, T., Guo, S., Barcelos, I.D., Milošević, M.V., Withers, F., Christianen, P.C.M., 2022. Distinctive gfactor of Moiré-Confined Excitons in van der Waals Heterostructures. Nano Lett. 22, 8641–8646. https://doi.org/10.1021/acs.nanolett.2c03008.
- Haley, K.L., Lee, N.F., Schreiber, V.M., Pereira, N.T., Sterbentz, R.M., Chung, T.Y., Island, J.O., 2024. Isolation and characterization of atomically thin mica phyllosilicates. ACS Appl. Nano Mater. 7, 25233–25240. https://doi.org/10.1021/ acsam 4c05338
- Hendricks, S.B., Jefferson, M.E., 1939. Polymorphism of the micas with optical measurements. J. Mineral. Soc. Am. 24, 729–771.
- Illarionov, Y.Y., Knobloch, T., Jech, M., Lanza, M., Akinwande, D., Vexler, M.I., Mueller, T., Lemme, M.C., Fiori, G., Schwierz, F., Grasser, T., 2020. Insulators for 2D nanoelectronics: the gap to bridge. Nat. Commun. 11, 3385. https://doi.org/ 10.1038/s41467-020-16640-8.
- Janica, I., Del Buffa, S., Mikołajczak, A., Eredia, M., Pakulski, D., Ciesielski, A., Samorì, P., 2018. Thermal insulation with 2D materials: liquid phase exfoliated

- vermiculite functional nanosheets. Nanoscale 10, 23182–23190. https://doi.org/
- Kawahala, N.M., Matos, D.A., de Oliveira, R., Longuinhos, R., Ribeiro-Soares, J., Barcelos, I.D., Hernandez, F.G.G., 2025. Shaping terahertz waves using anisotropic shear modes in a van der Waals mineral. NPJ 2D Mater. Appl. 9, 16. https://doi.org/ 10.1038/s41699-025-00540-w.
- Khan, M.Z., Peil, O.E., Sharma, A., Selyshchev, O., Valencia, S., Kronast, F., Zimmermann, M., Aslam, M.A., Raith, J.G., Teichert, C., Zahn, D.R.T., Salvan, G., Matković, A., 2023. Probing magnetic ordering in air stable iron-rich Van der Waals minerals. Adv. Phys. Res. 2300070, 1–13. https://doi.org/10.1002/ apxr.202300070.
- Knobloch, T., Illarionov, Y.Y., Ducry, F., Schleich, C., Wachter, S., Watanabe, K., Taniguchi, T., Mueller, T., Waltl, M., Lanza, M., Vexler, M.I., Luisier, M., Grasser, T., 2021. The performance limits of hexagonal boron nitride as an insulator for scaled CMOS devices based on two-dimensional materials. Nat. Electron. 4, 98–108. https://doi.org/10.1038/s41928-020-00529-x.
- Kou, L., Ma, Y., Sun, Z., Heine, T., Chen, C., 2017. Two-dimensional topological insulators: progress and prospects. J. Phys. Chem. Lett. 8, 1905–1919. https://doi. org/10.1021/acs.jpclett.7b00222.
- org/10.1021/acs.jpciett./b00222. Kubelka, P., Munk, F., 1931. An article on optics of paint layers. Z. Phys. 12, 259–274.
- Lemme, M.C., Akinwande, D., Huyghebaert, C., Stampfer, C., 2022. 2D materials for future heterogeneous electronics. Nat. Commun. 13, 1392. https://doi.org/10.1038/ s41467-022-29001-4.
- Loh, E., 1973. Optical vibrations in sheet silicates. J. Phys. C Solid State Phys. 6, 1091–1104. https://doi.org/10.1088/0022-3719/6/6/022.
- Longuinhos, R., Cadore, A.R., Bechtel, H.A., J S De Matos, C., Freitas, R.O., Ribeiro-Soares, J., Barcelos, I.D., 2023. Raman and Far-infrared synchrotron nanospectroscopy of layered crystalline talc: vibrational properties, interlayer coupling, and symmetry crossover. J. Phys. Chem. C 127, 5876–5885. https://doi.org/10.1021/acs.jpcc.3c00017.
- Lopez-Richard, V., Filgueira e Silva, I.R., Ames, A., Sousa, F.B., Teodoro, M.D., Barcelos, I.D., de Oliveira, R., Cadore, A.R., 2025. The emergence of mem-emitters. Nano Lett. 25, 1816–1822. https://doi.org/10.1021/acs.nanolett.4c04586.
- Lutterotti, L., Matthies, S., Wenk, H.-R., Schultz, A.S., Richardson, J.W., 1997. Combined texture and structure analysis of deformed limestone from time-of-flight neutron diffraction spectra. J. Appl. Phys. 81, 594–600. https://doi.org/10.1063/1.364220.
- Mahapatra, P.L., Tromer, R., Pandey, P., Costin, G., Lahiri, B., Chattopadhyay, K., PM, A., Roy, A.K., Galvao, D.S., Kumbhakar, P., Tiwary, C.S., 2022. Synthesis and characterization of biotene: a new 2D natural oxide from biotite. Small 18, 2201667. https://doi.org/10.1002/smll.202201667.
- Mahapatra, P.L., Singh, A.K., Tromer, R., K, R., A, M., Costin, G., Lahiri, B., Kundu, T.K., Ajayan, P.M., Altman, E.I., Galvao, D.S., Tiwary, C.S., 2023. Energy harvesting using two-dimensional (2D) d-silicates from abundant natural minerals. J. Mater. Chem. C Mater. 11, 2098–2106. https://doi.org/10.1039/D2TC04605A.
- Mahapatra, P.L., Costin, G., Galvao, D.S., Lahiri, B., Glavin, N., Roy, A.K., Ajayan, P.M., Tiwary, C.S., 2024a. A comprehensive review of atomically thin silicates and their applications. 2d Mater. 11, 032003. https://doi.org/10.1088/2053-1583/ad569b.
- Mahapatra, P.L., de Oliveira, C.C., Costin, G., Sarkar, S., Autreto, P.A.S., Tiwary, C.S., 2024b. Paramagnetic two-dimensional silicon-oxide from natural silicates. 2d Mater. 11, 015019. https://doi.org/10.1088/2053-1583/ad10b9.
- Makula, P., Pacia, M., Macyk, W., 2018. How to correctly determine the band gap energy of modified semiconductor photocatalysts based on UV-Vis spectra. J. Phys. Chem. Lett. 9, 6814-6817, https://doi.org/10.1021/acs.inclett.8b02802
- Lett. 9, 6814–6817. https://doi.org/10.1021/acs.jpclett.8b02892.
 Mania, E., Alencar, A.B., Cadore, A.R., Carvalho, B.R., Watanabe, K., Taniguchi, T.,
 Neves, B.R.A., Chacham, H., Campos, L.C., 2017. Spontaneous doping on high
 quality talc-graphene-hBN van der Waals heterostructures. 2d Mater. 4, 031008.
 https://doi.org/10.1088/2053-1583/aa76f4.
- Maslova, M.V., Gerasimova, L.G., Forsling, W., 2004. Surface properties of cleaved mica. Colloid J. 66, 364–371. https://doi.org/10.1023/B:COLL.0000030843.30563.c9.
- Matković, A., Ludescher, L., Peil, O.E., Sharma, A., Gradwohl, K.-P., Kratzer, M., Zimmermann, M., Genser, J., Knez, D., Fisslthaler, E., Gammer, C., Lugstein, A., Bakker, R.J., Romaner, L., Zahn, D.R.T., Hofer, F., Salvan, G., Raith, J.G., Teichert, C., 2021. Iron-rich talc as air-stable platform for magnetic two-dimensional materials. NPJ 2D Mater. Appl. 5, 94. https://doi.org/10.1038/s41699-021-00276-
- Mogg, L., Hao, G.P., Zhang, S., Bacaksiz, C., Zou, Y.C., Haigh, S.J., Peeters, F.M., Geim, A. K., Lozada-Hidalgo, M., 2019. Atomically thin micas as proton-conducting membranes. Nat. Nanotechnol. https://doi.org/10.1038/s41565-019-0536-5.
- Novoselov, K.S., Jiang, D., Schedin, F., Booth, T.J., Khotkevich, V.V., Morozov, S.V., Geim, A.K., 2005. Two-dimensional atomic crystals. Proc. Natl. Acad. Sci. USA 102, 10451–10453. https://doi.org/10.1073/pnas.0502848102.
- Nutting, D., Prando, G.A., Severijnen, M., Barcelos, I.D., Guo, S., Christianen, P.C.M., Zeitler, U., Galvão Gobato, Y., Withers, F., 2021. Electrical and optical properties of transition metal dichalcogenides on talc dielectrics. Nanoscale 13, 15853–15858. https://doi.org/10.1039/D1NR04723J.
- Pacakova, B., Lahtinen-Dahl, B., Kirch, A., Demchenko, H., Osmundsen, V., Fuller, C.A., Chernyshov, D., Zakutna, D., Miranda, C.R., Raaen, S., Fossum, J.O., 2025. Naturally occurring 2D semiconductor with antiferromagnetic ground state. NPJ 2D Mater. Appl. 9, 38. https://doi.org/10.1038/s41699-025-00561-5.
- Pramanik, A., Mahapatra, P.L., Tromer, R., Xu, J., Costin, G., Li, C., Saju, S., Alhashim, S., Pandey, K., Srivastava, A., Vajtai, R., Galvao, D.S., Tiwary, C.S., Ajayan, P.M., 2024.

- Biotene: Earth-abundant 2D material as sustainable anode for Li/Na-ion battery. ACS Appl. Mater. Interfaces 16, 2417–2427. https://doi.org/10.1021/acsami.3c15664.
- Prando, G.A., Severijnen, M.E., Barcelos, I.D., Zeitler, U., Christianen, P.C.M., Withers, F., Galvão Gobato, Y., 2021. Revealing excitonic complexes in monolayer WS2 on Talc dielectric. Phys. Rev. Appl. 16, 64055. https://doi.org/10.1103/ PhysRevApplied.16.064055.
- Rancourt, D.G., Dang, M.Z., Lalonde, A.E., 1992. Mössbauer spectroscopy of tetrahedral Fe3+ in trioctahedral micas. Am. Mineral. 77, 34–43.
- Rausell-Colom, J.A., Sanz, J., Fernandez, M., Serratosa, J.M., 1979. Distribution of octahedral ions in phlogopites and biotites. In: Mortaland, M.M., Farmer, V.C. (Eds.), Developments in Sedimentology. Elsevier, Oxford, pp. 27–36. https://doi.org/ 10.1016/S0070-4571(08)70698-8.
- Ravel, B., Newville, M., 2005. ATHENA, ARTEMIS, HEPHAESTUS: data analysis for X-ray absorption spectroscopy using IFEFFIT. J. Synchrotron Radiat. 12, 537–541. https:// doi.org/10.1107/S0909049505012719.
- Redhammer, G.J., Beran, A., Schneider, J., Amthauer, G., Lottermoser, W., 2000. Spectroscopic and structural properties of synthetic micas on the annitesiderophyllite binary: Synthesis, crystal structure refinement, Mössbauer, and infrared spectroscopy. Am. Mineral. 85, 449–465. https://doi.org/10.2138/am-2000-0406
- Roberto de Toledo, J., Serati de Brito, C., Rosa, B.L.T., Cadore, A.R., Rabahi, C.R., Faria Junior, P.E., Ferreira de Brito, A.C., Ghiasi, T.S., Ingla-Aynés, J., Schüller, C., van der Zant, H.S.J., Reitzenstein, S., Barcelos, I.D., Dirnberger, F., Gobato, Y.G., 2025. Interplay of energy and charge transfer in WSe2/CrSBr heterostructures. Nano Lett. 25, 13212–13220. https://doi.org/10.1021/acs.nanolett.5c03150.
- Ross, M., Takeda, H., Wones, D.R., 1966. Mica polytypes: systematic description and identification. Science 151, 191–193.
- Santos, J.C.C., Barboza, A.P.M., Matos, M.J.S., Barcelos, I.D., Fernandes, T.F.D., Soares, E.A., Moreira, R.L., Neves, B.R.A., 2019. Exfoliation and characterization of a two-dimensional serpentine-based material. Nanotechnology 30, 445705. https:// doi.org/10.1088/1361-6528/ab3732.
- Singh, L., Singha, M., 2016. Vibrational spectroscopic study of muscovite and biotite layered phyllosilicates. Indian J. Pure Appl. Phys. 54, 116–122.
- Šontevska, V., Jovanovski, G., Makreski, P., 2007. Minerals from Macedonia. Part XIX. Vibrational spectroscopy as identificational tool for some sheet silicate minerals. J. Mol. Struct. 834–836, 318–327. https://doi.org/10.1016/j.molstruc.2006.10.026.
- Tolentino, H., Geraldes, R.R., Moreno, G.B.Z.L., Pinto, A.C., Bueno, C.S., Kofukuda, L.M., Sotero, A.P., Neto, A.C., Lena, F.R., Wilendorf, W.H., Baraldi, G.L., Luiz, S.A., Dias, C. S.B., Perez, C.A., Neckel, I.T., Galante, D., Teixeira, V.C., Hesterberg, D., 2021. X-ray microscopy developments at Sirius-LNLS: first commissioning experiments at the Carnauba beamline. In: Lai, B., Somogyi, A. (Eds.), X-Ray Nanoimaging: Instruments and Methods V. SPIE, p. 6. https://doi.org/10.1117/12.2596496.
- Tolentino, H.C.N., Geraldes, R.R., da Silva, F.M.C., Guaita, M.G.D., Camarda, C.M., Szostak, R., Neckel, I.T., Teixeira, V.C., Hesterberg, D., Pérez, C.A., Galante, D., Callefo, F., Neto, A.C.P., Kofukuda, L.M., Sotero, A.P.S., Moreno, G.B.Z.L., Luiz, S.A. L., Bueno, C.S.N.C., Lena, F.R., Westfahl, H., 2023. The CARNAÚBA X-ray nanospectroscopy beamline at the Sirius-LNLS synchrotron light source: Developments, commissioning, and first science at the TARUMA station. J. Electron. Spectros. Relat. Phenomena 266, 147340. https://doi.org/10.1016/j.
- Tripathi, R.P., Chandra, U., Chandra, R., Lokanathan, S., 1978. A Mössbauer study of the effects of heating biotite, phlogopite and vermiculite. J. Inorg. Nucl. Chem. 40, 1293–1298. https://doi.org/10.1016/0022-1902(78)80037-2.
- Ulian, G., Valdrè, G., 2023. Crystal-chemical, vibrational and electronic properties of 1M-phlogopite K(Mg,Fe)3Si3AlO10(OH)2 from Density Functional Theory simulations. Appl. Clay Sci. 246, 107166. https://doi.org/10.1016/j.clay.2023.107166.
- Vasic, B., Czibula, C., Kratzer, M., Neves, B.R.A., Matkovic, A., Teichert, C., 2021. Two-dimensional talc as a van der Waals material for solid lubrication at the nanoscale. Nanotechnology 127, 69–73. https://doi.org/10.1088/1361-6528/abeffe.
- Wang, A., Freeman, J.J., Jolliff, B.L., 2015. Understanding the Raman spectral features of phyllosilicates. J. Raman Spectrosc. 46, 829–845. https://doi.org/10.1002/jrs.4680.
- phyllosilicates. J. Raman Spectrosc. 46, 829–845. https://doi.org/10.1002/jrs.4680. Wei, C., Roy, A., Tripathi, M., Aljarid, A.K.A., Salvage, J.P., Roe, S.M., Arenal, R., Boland, C.S., 2023. Exotic electronic properties of 2D nanosheets isolated from liquid phase exfoliated phyllosilicate minerals. Adv. Mater. 35, 2303570. https://doi.org/10.1002/adma.202303570.
- Woźniak, T., Faria Junior, P.E., Seifert, G., Chaves, A., Kunstmann, J., 2020. Exciton g factors of van der Waals heterostructures from first-principles calculations. Phys. Rev. B 101, 235408. https://doi.org/10.1103/PhysRevB.101.235408.
- Zheng, Y.L., Zhao, X.B., Zhao, Q.H., Li, J.C., Zhang, Q.B., 2020. Dielectric properties of hard rock minerals and implications for microwave-assisted rock fracturing. Geomech. Geophys. Geo-Energy Geo-Resour. 6, 22. https://doi.org/10.1007/ s40948-020-00147-z.
- Zhu, K., Pazos, S., Aguirre, F., Shen, Y., Yuan, Y., Zheng, W., Alharbi, O., Villena, M.A., Fang, B., Li, X., Milozzi, A., Farronato, M., Muñoz-Rojo, M., Wang, T., Li, R., Fariborzi, H., Roldan, J.B., Benstetter, G., Zhang, X., Alshareef, H.N., Grasser, T., Wu, H., Ielmini, D., Lanza, M., 2023. Hybrid 2D–CMOS microchips for memristive applications. Nature 618, 57–62. https://doi.org/10.1038/s41586-023-05973-1.
- Zou, Y.-C., Mogg, L., Clark, N., Bacaksiz, C., Milovanovic, S., Sreepal, V., Hao, G.-P., Wang, Y.-C., Hopkinson, D.G., Gorbachev, R., Shaw, S., Novoselov, K.S., Raveendran-Nair, R., Peeters, F.M., Lozada-Hidalgo, M., Haigh, S.J., 2021. Ion exchange in atomically thin clays and micas. Nat. Mater. 20, 1677–1682. https://doi.org/10.1038/s41563-021-01072-6.